



**HAL**  
open science

## **Strontium incorporation into biomimetic carbonated calcium-deficient hydroxyapatite coated carbon cloth: biocompatibility with human primary osteoblasts**

Florian Olivier, N. Rochet, Sandrine Delpoux Delpoux-Ouldriane, Jérôme Chancolon, V. Sarou-Kanian, F. Fayon, S. Bonnamy

### ► To cite this version:

Florian Olivier, N. Rochet, Sandrine Delpoux Delpoux-Ouldriane, Jérôme Chancolon, V. Sarou-Kanian, et al. Strontium incorporation into biomimetic carbonated calcium-deficient hydroxyapatite coated carbon cloth: biocompatibility with human primary osteoblasts. *Materials Science and Engineering: C*, 2020, 116, pp.111192. 10.1016/j.msec.2020.111192 . hal-03008544

**HAL Id: hal-03008544**

**<https://hal.science/hal-03008544>**

Submitted on 16 Nov 2020

**HAL** is a multi-disciplinary open access archive for the deposit and dissemination of scientific research documents, whether they are published or not. The documents may come from teaching and research institutions in France or abroad, or from public or private research centers.

L'archive ouverte pluridisciplinaire **HAL**, est destinée au dépôt et à la diffusion de documents scientifiques de niveau recherche, publiés ou non, émanant des établissements d'enseignement et de recherche français ou étrangers, des laboratoires publics ou privés.

Strontium incorporation into biomimetic carbonated calcium-deficient hydroxyapatite coated carbon cloth: biocompatibility with human primary osteoblasts

**F. Olivier<sup>1</sup>, N. Rochet<sup>2</sup>, S. Delpeux-Ouldriane<sup>1</sup>, J. Chancolon<sup>1</sup>, V. Sarou-Kanian<sup>3</sup>, F. Fayon<sup>3</sup>, S. Bonnamy<sup>1</sup>**

<sup>1</sup>CNRS, ICMN UMR 7374, Univ. Orléans, Orléans, France

<sup>2</sup>Univ. Côte d'Azur, CNRS, Inserm, iBV, Nice, France

<sup>3</sup>CNRS, CEMHTI UPR 3079, Univ. Orléans, Orléans, France

## **ABSTRACT**

It has already been shown that sono-electrodeposition can be used to coat activated carbon fiber cloth (ACC) with calcium phosphates (CaP) and we recently demonstrated that cathodic polarization at -1 V / Hg/Hg<sub>2</sub>SO<sub>4</sub> was the best parameter to obtain a carbonated calcium deficient hydroxyapatite (CDA) coating with optimal uniformity and homogeneity. In the present study, we investigated whether this technique was suitable to dope this carbonated CDA coating by partial substitution with another bivalent cation such as strontium. We show here that a strontium-substituted carbonated CDA coating can be produced and quantitatively controlled up to at least 10 at.%. In this range we demonstrate that the presence of strontium does not modify either the textural or the structural properties of the carbonated CDA. Owing to the well-known effect of both carbonated CDA and strontium in bone formation, the biocompatibility of ACC coated or not with carbonated CDA or with strontium substituted carbonated CDA was tested using primary human osteoblasts. Our data revealed a positive and dose-dependent effect of strontium addition on osteoblast activity and proliferation. In conclusion, we show here that electrodeposition at -1 V is a suitable and easy process to incorporate cations of biological interest into CaP coating.

Keywords: Activated carbon fiber cloth, Calcium-deficient hydroxyapatite, Strontium substitution, Sono-electrodeposition, Human primary osteoblast, Cell proliferation.

## 1. Introduction

The structure of the bone mineral phase is similar to that of nanocrystalline calcium phosphate (CaP) apatites [1], partially enriched with a large variety of substitution ions such as Na, K, Mg, Sr, Cl, F, Zn. These trace elements, and specifically the strontium (Sr), play a role in bone mineral phase remodeling [2]. Therefore, it has been proposed to dope synthetic apatitic bone substitutes used in orthopedic surgery with small amounts of such ions. Moreover, it has been shown that incorporation of  $\text{Sr}^{2+}$ ,  $\text{Mg}^{2+}$ ,  $\text{F}^-$ ,  $\text{Cl}^-$  or  $\text{CO}_3^{2-}$  in the crystal structure of apatites improves their biological behavior [3–6]. For examples, these ionic incorporation have a potential role in cell adhesion, biomineralization, bone metabolism and resorption processes [7].

Interestingly, calcium ion (Ca), with an ionic radius of 1.00 Å, can be easily substituted in the apatitic structure by strontium, which has an ionic radius of 1.18 Å [8–11]. Strontium appears as an ion of choice to impart new properties to CaP since many studies have shown that this cation promotes bone tissue growth and decreases bone resorption without altering neither the mineralization process nor its chemical composition [12–14]. The degree of substitution depends mainly on the initial concentration of strontium (precursor solution) from 0 to 100 % [12]. Moreover, strontium incorporation into bioceramics between 3 to 7 at.% stimulates pre-osteoblast activity and differentiation, inhibits osteoclast activity and differentiation and is used in osteoporosis treatment [15–17]. However, it has being shown that strontium substitution has a dose-dependent impact on bone formation [18,19]. A recent study has showed that 10 at.% of strontium corresponds to the critical substitution rate into the biomimetic apatite [20]. These authors showed that using higher amount leads to the formation of a stable strontium-apatite phase that may induce high-dose related pathologies. Furthermore, it has been shown that incorporation of strontium has an influence on the mechanical properties of apatite. Increases in compressive strength and hardness were measured for a strontium substitution of less than 10 at.% [21,22].

As for the synthesis of doped CaP, several methods can be used such as sol-gel [23,24], precipitation [5,25], hydrothermal [26], micro-arc [27], pulsed-laser [16,28] and pulsed electro-deposition [29,30]. Several of these processes have thus been proposed for prosthesis coating with a doped CaP layer. The major use of CaP materials in the orthopedic field consists in prosthesis coating to improve their integration in the host body [31,32]. Among these techniques, electrodeposition has been used to perform CaP coatings or doped CaP coatings on conducting metallic alloys [30]. Electrodeposition is a soft chemical process, performed at room temperature, in a water-based electrolyte. It consists in a controlled co-precipitation of calcium ions and/or other divalent cations and phosphate ions on the surface of a conducting electrode. In most cases, electrodeposition is used to perform a CaP coating on rigid metallic substrates such as stainless steel [33], titanium [34,35], magnesium [36], and cobalt [37] alloys or flexible substrates such as carbon mesh [38]. Carbon mesh, carbon fibers and activated carbon fiber cloth (ACC) are biocompatible and bioinert materials [39–43] that are often proposed not as a support but as a material designed to improve the mechanical properties of apatites for bone regeneration [44–49].

In a previous work, the sono-electrodeposition process was optimized for the coating of activated carbon cloth with calcium-deficient hydroxyapatite [50]. We showed that using this process the thickness, morphology, microtexture, chemical composition and structure of the CaP coatings could be tailored. After optimization of the experimental conditions, carbonated calcium-deficient hydroxyapatite (CDA), which displays a homogeneous plate-like microtexture, was deposited on ACC. The aim of the present study was, firstly, to explore whether combining ACC and Sr-doped CaP coatings using sono-electrodeposition yielded a hybrid material. To achieve this, we investigated the effect of strontium addition (< 10 at.%) on the chemical, morphological and structural characteristics of the hydroxyapatite phases synthesized. Then, we investigated the biocompatibility and cell activity of different CaP coated materials (with and without strontium incorporation), *in vitro*, on human primary osteoblasts.

## 2. Materials and methods

### 2.1. Activated carbon fiber cloth

The substrate consisted of an activated carbon fiber cloth (ACC) referred to as FM50K. The FM50K prepared from a viscose precursor was supplied by the Zorflex® Company. Prior to its use, the ACC substrate was washed with boiling distilled water using a Soxhlet® extractor to remove any traces of contaminants coming from the activation and carbonization steps leading to its manufacturing. After 12 hours of washing, it was dried at 70 °C under vacuum.

### 2.2. Synthesis of the xSr-CaP coatings on activated carbon fiber cloth

The xSr-CaP coating (x being the strontium ratio in the electrolyte) on ACC was obtained by sono-electrodeposition under cathodic polarization. The electrolyte consisted of a mixture of calcium nitrate tetrahydrate  $\text{Ca}(\text{NO}_3)_2 \cdot 4\text{H}_2\text{O}$  (Sigma-Aldrich, BioXtra, purity 99.0 %), strontium nitrate  $\text{Sr}(\text{NO}_3)_2$  (Sigma-Aldrich, ACS reagent, purity 99.0 %) and ammonium dihydrogenophosphate  $\text{NH}_4\text{H}_2\text{PO}_4$  (Alfa Aesar, purity 98.0 %), maintaining a Ca/P or (Ca+Sr)/P ratio of 1.67, with  $[\text{Ca}^{2+}]$  or  $[\text{Ca}^{2+} + \text{Sr}^{2+}] = 5 \text{ mmol/L}$  at pH = 4.8 and at 70 °C. Different Sr/(Sr+Ca) ratios in the electrolyte were considered: 0, 5 and 10 at.% (samples respectively named 0Sr-CaP, 5Sr-CaP and 10Sr-CaP). An electrochemical cell was homemade to use ACC (FM50K) as the working electrode, a platinum basket surrounding the ACC was used as the counter electrode and Hg/Hg<sub>2</sub>SO<sub>4</sub> (Radiometer analytical, France) was used as the reference electrode. The cathodic polarization of the carbon electrode was performed using a potentiostat/galvanostat (Biologic Science Instruments VMP-2, France) with a constant potential of -1 V/Hg/Hg<sub>2</sub>SO<sub>4</sub>, which is the theoretical barrier potential of water reduction at initial pH = 4.8. Sonication (35 kHz, 30 %) was applied during polarization (ultrasonic bath, Transsonic Ti-H-10, Fisher Scientific France). Using this procedure, three materials were synthesized (materials 2 to 4), which are listed in Table 1.

**Table 1.** The investigated materials as a function of the electrolyte composition. **(2-column fitting image)**

Electrolyte composition	Material 1	Material 2	Material 3	Material 4
-------------------------	------------	------------	------------	------------

[Ca] mmol/L	-	5	4.75	4.5
[Sr] mmol/L	-	0	0.25	0.5
[P] mmol/L	-	3	3	3
	<b>FM50K</b>	<b>FM50K + 0Sr-CaP</b>	<b>FM50K + 5Sr-CaP</b>	<b>FM50K + 10Sr-CaP</b>

### 2.3. Characterization techniques of materials

The characteristics of the ACC substrate and the xSr-CaP coatings were analyzed using several techniques.

Elemental analysis (weight %) of C and O were determined using a Flash 2000 (CHON-S) analyzer (Thermo Scientific France).

The porosity was characterized by N<sub>2</sub> and CO<sub>2</sub> adsorption respectively at 77 K and 273 K, using an Autosorb-1 (Quantachrome). The total pore volume was estimated from the amount adsorbed at P/P<sub>0</sub> = 0.95. The micropore (pore size < 2nm) and mesopore (2 nm < pore size < 50 nm) volumes were determined by applying the density functional theory (DFT) method to the N<sub>2</sub> isotherms assuming a slit pore shape. The Dubinin–Radushkevich (DR) theory was applied to the CO<sub>2</sub> adsorption isotherm at 0 °C to estimate the volume of ultramicropores (pore size < 0.7 nm). The pK<sub>A</sub> distribution of functional groups grafted on the ACC surface and the pH<sub>PZC</sub> (pH value corresponding to an ACC net charge of zero) were measured by potentiometric titration with NaOH (0.1 mol/L), using a very low incremental volume (0.01 ml) in a wide range of pH = 3-11. The pore size distribution was measured by mercury intrusion porosimetry using a Poresizer 9320 porosimeter (Micromeritics). The mesopore and macropore sizes ranged from 4 nm to 350 μm.

The xSr-CaP coating morphology and thickness were investigated by scanning electron microscopy (SEM-Hitachi S4500) operating at 5 kV. To determine the microtexture of the xSr-CaP coatings, transmission electron microscopy (TEM) images were acquired with a TEM-PHILIPS CM20 operating at 200 kV. For sample preparation, 1 mg of coating was scraped from the carbon surface, dispersed in ethanol and sonicated for 30 sec; a droplet of the suspension was deposited on an amorphous carbon coated copper grid (Electron

Microscopy Sciences). Ca/P and Ca+Sr/P atomic ratios were determined by Energy Dispersive X-ray Spectroscopy (EDS) analysis performed in SEM at 10 kV and in TEM at 200 kV. The atomic ratios were calculated from the intensities of the Ca peak ( $K\alpha$  Ca = 3.691 keV), P peak ( $K\alpha$  P = 2.015 keV) and Sr peak ( $K\alpha$  Sr = 14.164 keV) present in the SEM-EDS or TEM-EDS spectra.

The strontium concentration present in xSr-CaP coatings was measured by microwave plasma atomic emission spectroscopy (MP-AES) using a 4200 MP-AES Agilent Technologies. For that, the material (ACC/xSr-CaP) was immersed in a 35 % nitric acid solution (Sigma Aldrich®) for 3 h. Supernatant containing the xSr-CaP was diluted to a concentration of 0.5 % nitric acid to prevent the formation of oxides. The solution obtained was sprayed into a nitrogen plasma which reached the temperature of 5000 °C. At this temperature, the atoms in the nebulized sample were dissociated, atomized, ionized and excited. The emitted photons were measured using optical detection at the characteristic wavelengths of the elements of interest ( $\lambda_{Ca}$  = 393.366 nm and  $\lambda_{Sr}$  = 407.771 nm) in order to quantify the elements of interest in the liquid solution by comparing the signal measured with the calibration curve.

The chemical composition of the xSr-CaP coatings was analyzed by Fourier transform infrared spectroscopy (FTIR). Spectra were acquired in transmission mode using a Nicolet 6700 spectrometer on KBr pellets in the range of 4000-400  $cm^{-1}$  (resolution = 4  $cm^{-1}$ , 256 scans). Pellets were prepared by admixing 1 mg of ACC/xSr-CaP hybrid materials with 99 mg of KBr.

The crystallographic structure of the xSr-CaP coatings was analyzed by X-Ray diffraction (XRD), using an INEL diffractometer (CSP120), working at 40 kV and 30 mA ( $Cu K\alpha$  = 1.5418978 Å). Data were collected in the range  $2\theta = 10^\circ-80^\circ$ , with a curve detector (angular instrumental resolution of 0.05°), in transmission mode, using a Si(111) monochromator. To determine the lattice parameters of xSr-CaP crystalline phases, refinements were performed by the Le Bail method using the Jana2006 software.

Solid-state nuclear magnetic resonance (NMR) experiments were performed on a Bruker Avance I spectrometer operating at a magnetic field of 7.0 T ( $^1\text{H}$  and  $^{31}\text{P}$  Larmor frequencies of 300.13 MHz and 121.50 MHz, respectively), equipped with a 4 mm magic-angle spinning (MAS) NMR probehead. The  $^{31}\text{P}$  1D quantitative MAS,  $\{^1\text{H}\}$ - $^{31}\text{P}$  cross-polarization (CP) MAS and 2D  $\{^1\text{H}\}$ - $^{31}\text{P}$  heteronuclear correlation spectra were recorded at a sample spinning frequency of 10 kHz.  $^1\text{H}$  and  $^{31}\text{P}$  NMR chemical shifts were referenced to TMS and  $\text{H}_3\text{PO}_4$  in solution (85 %), respectively.

#### 2.4. *In vitro* biological procedures

The human primary osteoblasts were purchased from PromoCell (Heidelberg, Germany). They were expanded on plastic culture flasks in complete medium constituted of  $\alpha$ -MEM medium (LONZA, Emerainville, France) supplemented with 10 % fetal calf serum (EUROBIO, Courtaboeuf, France), 100 U/ml penicillin, 100 U/ml streptomycin (Gibco Thermo Fisher Scientific, France), 2 % ultraglutamine (LONZA) and incubated at 37 °C under 5 %  $\text{CO}_2$ . Four materials were tested, namely FM50K, FM50k+0Sr-CaP, FM50K+5Sr-CaP and FM50K+10Sr-CaP. Material patches of 8 mm diameter were pre-incubated in 48-well culture plates in completed medium for 24 h. Human primary osteoblasts were then seeded at a density of 7000 cells/well. After 2 and 4 days, cell viability and proliferation were analyzed. Each material was tested in triplicate.

Cell viability was assessed using the fluorescent assay LIVE/DEAD™ Viability/Cytotoxicity Kit (Life Technologies SAS, France). At each endpoint ACC patches were gently washed with phosphate-buffered saline (PBS) and incubated at room temperature with PBS containing 2  $\mu\text{mol/L}$  calcein-AM and 4  $\mu\text{mol/L}$  ethidium-homodimer-1. Calcein-AM is a nonfluorescent cell-permeant fluorescein derivative, which is converted by cellular esterase activity into cell-impermeant and highly fluorescent calcein. Calcein accumulates inside live cells having intact membranes, which results in a green fluorescent signal. Ethidium-homodimer-1 enters dead cells with damaged membranes and undergoes a 40-fold enhancement of fluorescence upon binding to their DNA, leading to a red fluorescent signal. After 20 min incubation, the

ACC patches were put onto a glass slide, covered with a coverslip and viewed under a fluorescence microscope (Zeiss Observer Z1 with FITC filters and Texas Red) equipped with FITC and Texas Red filters. The number of live and dead cells was estimated using the ImageJ Software.

## 2.5. Statistical analysis

Quantification of strontium rates in *in vitro* results are expressed as a mean  $\pm$  standard deviation of independent experiments. Differences between *in vitro* results were statistically analyzed using Student test and differences were considered statistically significant at \* $p < 0.05$ , \*\* $p < 0.01$  and \*\*\* $p < 0.001$ .

## 3. Results

### 3.1. Activated carbon fiber cloth characterization

The ACC material is made of twisted carbon fiber threads and the threads are knitted to form a flexible material (Fig. 1 (a)). The carbon fibers are 8-12  $\mu\text{m}$  in diameter and have a lobed shape, as presented in the SEM images (Fig. 1 (b) and (c)). A heterogeneous sizing (coated during the industrial process) on the carbon surface is observed. The EDS analysis of the sizing shows the presence of aluminum and zinc on the carbon fiber surface (Fig. 1 (d)).

FM50K exhibits a narrow pore size distribution centered around 1 nm, with mainly ultramicropores of less than 0.7 nm and micropores of 0.7 to 2 nm. A negligible amount of mesopores (2 to 50 nm) is observed, representing less than 20 % of the total pore volume (Fig. 1 (e)). The mercury intrusion porosimetry curve reveals a distribution of macropores between 0.8  $\mu\text{m}$  and 450  $\mu\text{m}$ . The maximum of pore distribution at 95  $\mu\text{m}$  corresponds to the average size of spaces between carbon fiber twists (Fig. 1 (f)). A pore size distribution between 0.8 and 60  $\mu\text{m}$  is characteristic of different spaces between fibers of the same twist. Data show that FM50K is a material with a multi-scale porosity.

The chemical and textural characteristics of FM50K are reported in Table 2. The surface chemistry characterization shows that the ACC substrate is slightly hydrophilic with 80.6 wt%

C and a rather high oxygen content (4.8 wt%). Its  $pH_{PZC}$  (pH value corresponding to an ACC net charge of zero) is almost neutral (7.8) and its pKa distribution of functional groups presents mainly acidic functional groups (2.93).

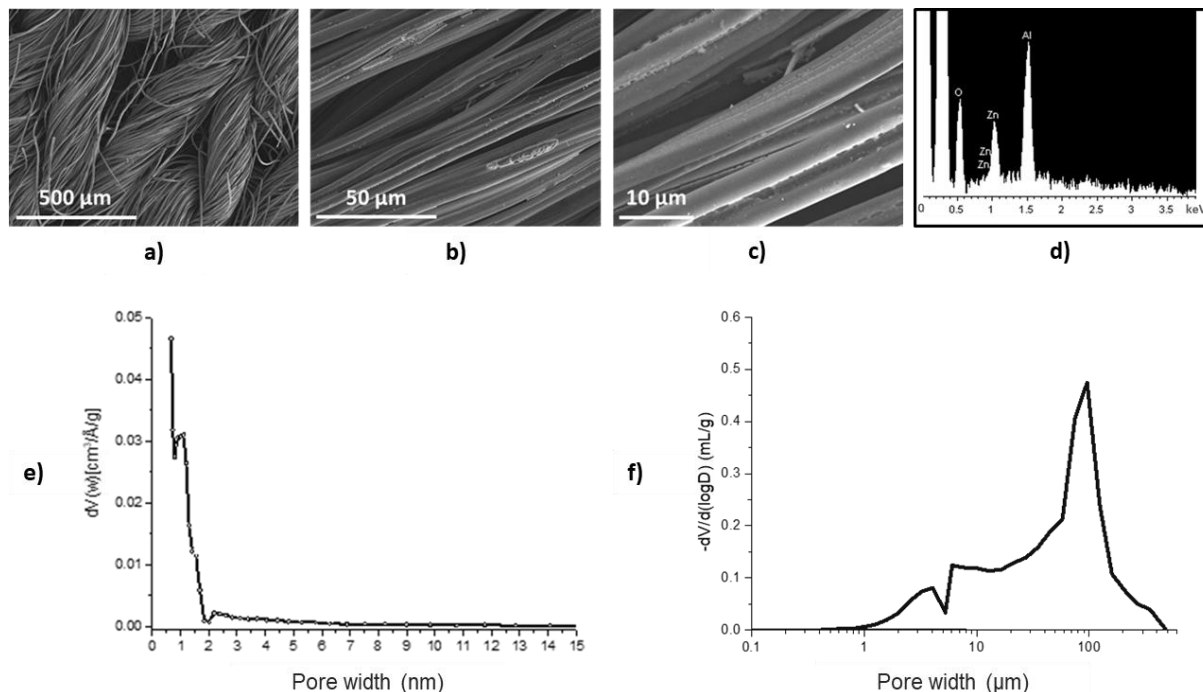


**Fig. 1.** SEM images of pristine activated carbon fiber cloth (FM50K) at three magnifications: a) x100, b) x1000, c) x3000 and d) the EDS analysis of carbon fiber surface e) Pore size distribution of FM50K measured by  $N_2$  adsorption at 77 K f) Pore size distribution of FM50K measured by mercury intrusion porosimetry. **(2-column fitting image)**

**Table 2.** Chemical and textural characteristics of FM50K. **(2-column fitting image)**

Elemental analysis (mass.%)			pKa distribution (mmol/g)			N <sub>2</sub> and CO <sub>2</sub> adsorption			
% C	% O	pH <sub>PZC</sub>	3 < pKa < 7	7 < pKa < 1	Acidic functional groups	V <sub>micro</sub> <sup>1</sup> N <sub>2</sub> , DFT cm <sup>3</sup> /g	V <sub>meso</sub> <sup>1</sup> N <sub>2</sub> , DFT cm <sup>3</sup> /g	V <sub>ultramicro</sub> <sup>2</sup> CO <sub>2</sub> , DR cm <sup>3</sup> /g	V <sub>total</sub> cm <sup>3</sup> /g
80.6	4.8	7.8	2.13	0.80	2.93	0.41	0.07	0.55	0.51

<sup>1</sup>The microporous and mesoporous volumes were determined by applying the density functional theory method (DFT) to the  $N_2$  adsorption isotherms.

<sup>2</sup> The ultramicroporous volume was determined by applying the Dubinin-Radushkevich theory (DR) to the  $CO_2$  adsorption isotherm.

### 3.2. Calcium phosphate coating characterization

SEM micrographs show the occurrence of similar morphologies for xSr-CaP coatings deposited by sono-electrodeposition, independently of the strontium ratio present in the electrolyte (Fig. 2 (a)-(d')). A uniform coating is observed for the three strontium ratios, with a plate-like morphology and a uniform thickness estimated around 1.5  $\mu\text{m}$ . Different observations suggest that the incorporation of strontium does not influence the thickness, uniformity or morphology of the coating.

TEM characterization did not reveal any difference in microtexture between coatings without (Fig. 2 (b'')) and with strontium (Fig. 2 (c'') and (d'')). The three coatings are composed of lamellar nanocrystals varying in size from a few tens to a few hundreds of nanometers. Due to the thinness of the nanocrystallites, a folding of their edges was often observed (white arrows).

The composition of the coatings was investigated by both SEM and TEM-EDS analyses. For all samples, the measured (Ca+Sr)/P molar ratio is 1.4, independent of the Sr content and significantly lower than that of the electrolyte solution (1.67). For the 5Sr-CaP coating, SEM and TEM-EDS analyses indicate a strontium concentration of  $4.1 \pm 0.6$  and  $3.0 \pm 0.5$  at.%, respectively. For the 10Sr-CaP coating, SEM and TEM-EDS measurements give a Sr content of  $6.8 \pm 0.8$  and  $6.6 \pm 0.8$  at.%, respectively. These values are in good agreement with those obtained by MP-AES ( $2.9 \pm 0.5$  and  $5.5 \pm 0.4$  for the 5Sr-CaP and 10Sr-CaP coating respectively). It can be concluded that Sr concentrations of 5 and 10 at.% in the electrolyte solution lead to Sr contents of about 3 and 6 at.% in the xSr-CaP coating, respectively (Table 3). Additional P, Ca and Sr EDS-SEM elemental maps (Fig. 2 (e)-(f)) reveal that the strontium is uniformly distributed in the obtained coatings. These results show that electrolyte strontium concentration until 10 at.% leads to the formation of xSr-CaP coating with a plate-like morphology constituted by lamellar nanocrystals and a constant Ca+Sr/P ratio of 1.4. These features are very similar to that reported for Sr-doped

stoichiometric HA (Ca/P = 1.67) obtained from precipitation in aqueous medium for which the Sr incorporation was found smaller than that expected from initial concentrations [51].

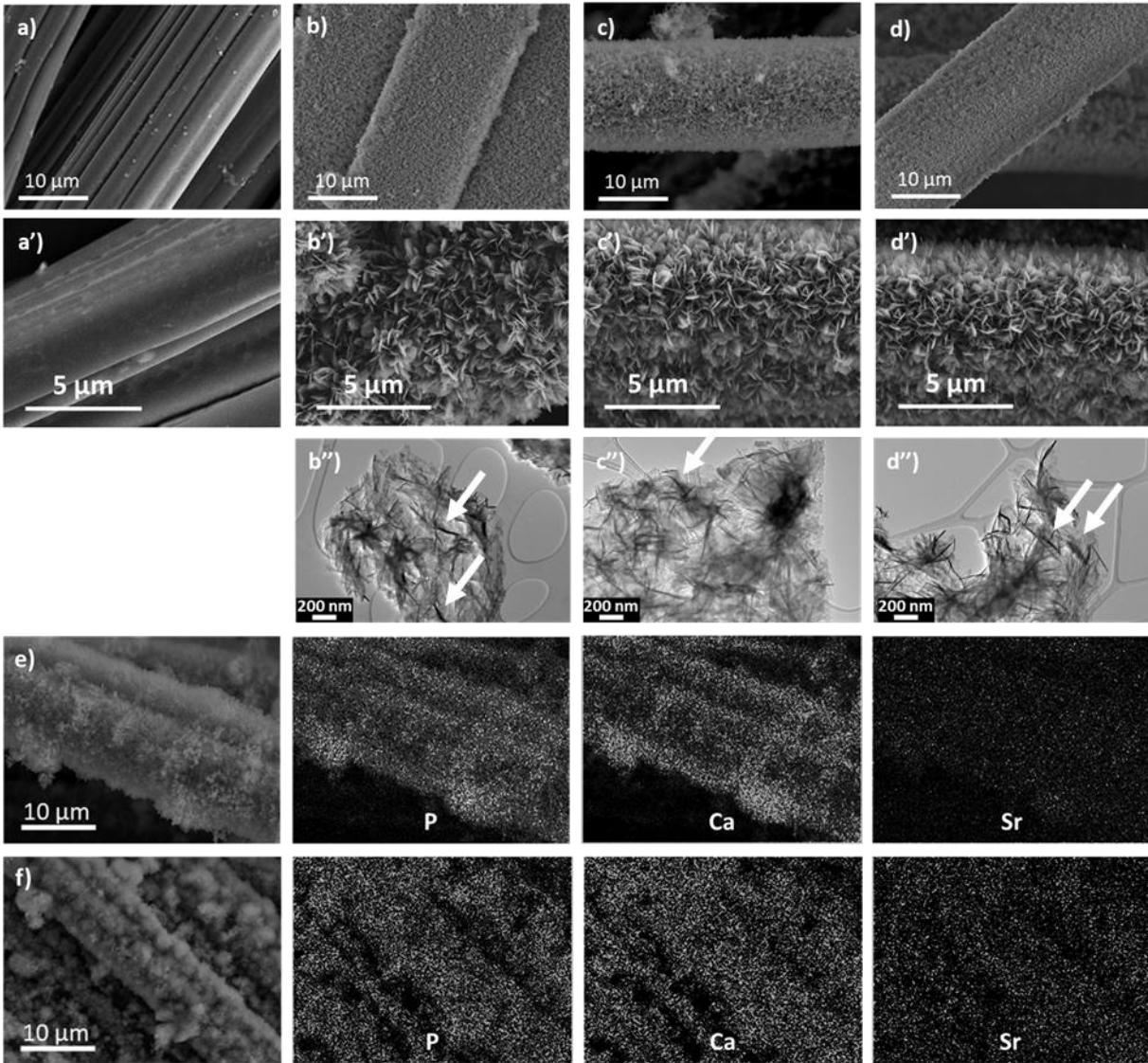


**Fig. 2.** SEM images of ACC with and without coatings: a and a') FM50K (ACC pristine), b and b') FM50K+0Sr-CaP, c and c') FM50K+5Sr-CaP and d and d') FM50K+10Sr-CaP. TEM images of corresponding coatings: b'') 0Sr-CaP, c'') 5Sr-CaP and d'') 10Sr-CaP; e), f) EDS-SEM elemental maps of P, Ca and Sr performed on 5Sr-CaP and 10Sr-CaP coatings. **(2-column fitting image)**

**Table 3.** Comparison of strontium concentrations (at.%) between the electrolytic solutions and the electrodeposited coatings obtained using different analysis techniques. **(2-column fitting image)**

Electrolytic solution		Coating	
Strontium concentration (at.%)	Analysis techniques	Strontium concentration (at.%)	$\frac{Ca + Sr}{P}$

0Sr-CaP	0		0	1.4 ± 0.1
5Sr-CaP	5	EDX-SEM	4.1 ± 0.6	1.4 ± 0.1
10Sr-CaP	10		6.8 ± 0.8	1.4 ± 0.1
0Sr-CaP	0		0	1.4 ± 0.1
5Sr-CaP	5	EDX-TEM	3.0 ± 0.5	1.4 ± 0.1
10Sr-CaP	10		6.6 ± 0.8	1.4 ± 0.1
0Sr-CaP	0		0	–
5Sr-CaP	5	MP-AES	2.9 ± 0.5	–
10Sr-CaP	10		5.5 ± 0.4	–

In order to better understand the effect of strontium incorporation on the chemical composition of the hydroxyapatite phase, FTIR analysis of non-doped and strontium-doped CaP coatings (samples respectively named 0Sr-CaP, 5Sr-CaP and 10Sr-CaP) was performed (Fig. 3.) The spectra of the three coatings obtained at constant potential are almost similar and are characteristic of AB-type calcium carbonated deficient hydroxyapatite (CDA), as described in previous papers [50]. However, the presence of strontium in the coatings leads to a slight shift in the 5Sr-CaP and 10Sr-CaP spectra. In the three spectra, four main absorption domains are identified and are detailed for the 0Sr-CaP coating (Fig. 3 (b) and (c)). The first domain, between 450-800  $\text{cm}^{-1}$ , consists of a double adsorption band located at 566 and 603  $\text{cm}^{-1}$  with a shoulder at 580  $\text{cm}^{-1}$ ; it is attributed to the  $\nu_4$  bending mode of apatitic  $\text{PO}_4^{3-}$ . The second shoulder observed at 633  $\text{cm}^{-1}$  is assigned to apatitic  $\text{OH}^-$  [52,53]. Other bands located at 535, 545 and 617  $\text{cm}^{-1}$  are attributed to non-apatitic  $\text{HPO}_4^{2-}$ , apatitic  $\text{PO}_4^{3-}$  and non-apatitic  $\text{PO}_4^{3-}$  [53]. The second domain, between 800 and 1300  $\text{cm}^{-1}$ , displays the most intense and broadest band centered at 1036  $\text{cm}^{-1}$  with the shoulder at 1094  $\text{cm}^{-1}$ . It is attributed to the  $\nu_3$  bending mode of apatitic  $\text{PO}_4^{3-}$ . The weak band located at 962  $\text{cm}^{-1}$  is assigned to the  $\nu_1$  mode of  $\text{PO}_4^{3-}$  [54]. The very weak absorption peak at 873  $\text{cm}^{-1}$  can be ascribed to the presence of  $\text{HPO}_4^{2-}$  and/or  $\text{CO}_3^{2-}$  ions [55]. The third domain, between 1300 and 1580  $\text{cm}^{-1}$ , shows a weak adsorption band at 1385  $\text{cm}^{-1}$  that reveals the presence of a small amount of  $\text{NO}_3^-$  ions in the CaP phase coming from the calcium nitrate precursor. The absorption bands between 1400 and 1580  $\text{cm}^{-1}$  indicate the existence of structural  $\text{CO}_3^{2-}$  and these  $\text{CO}_3^{2-}$  bands do not change with the evolution of the strontium rate [52,56]. The last

domain displays broad absorption bands between 1600 and 1700  $\text{cm}^{-1}$  and between 2800 and 3600  $\text{cm}^{-1}$ . They are assigned to structural water and adsorbed water bands, respectively [57].

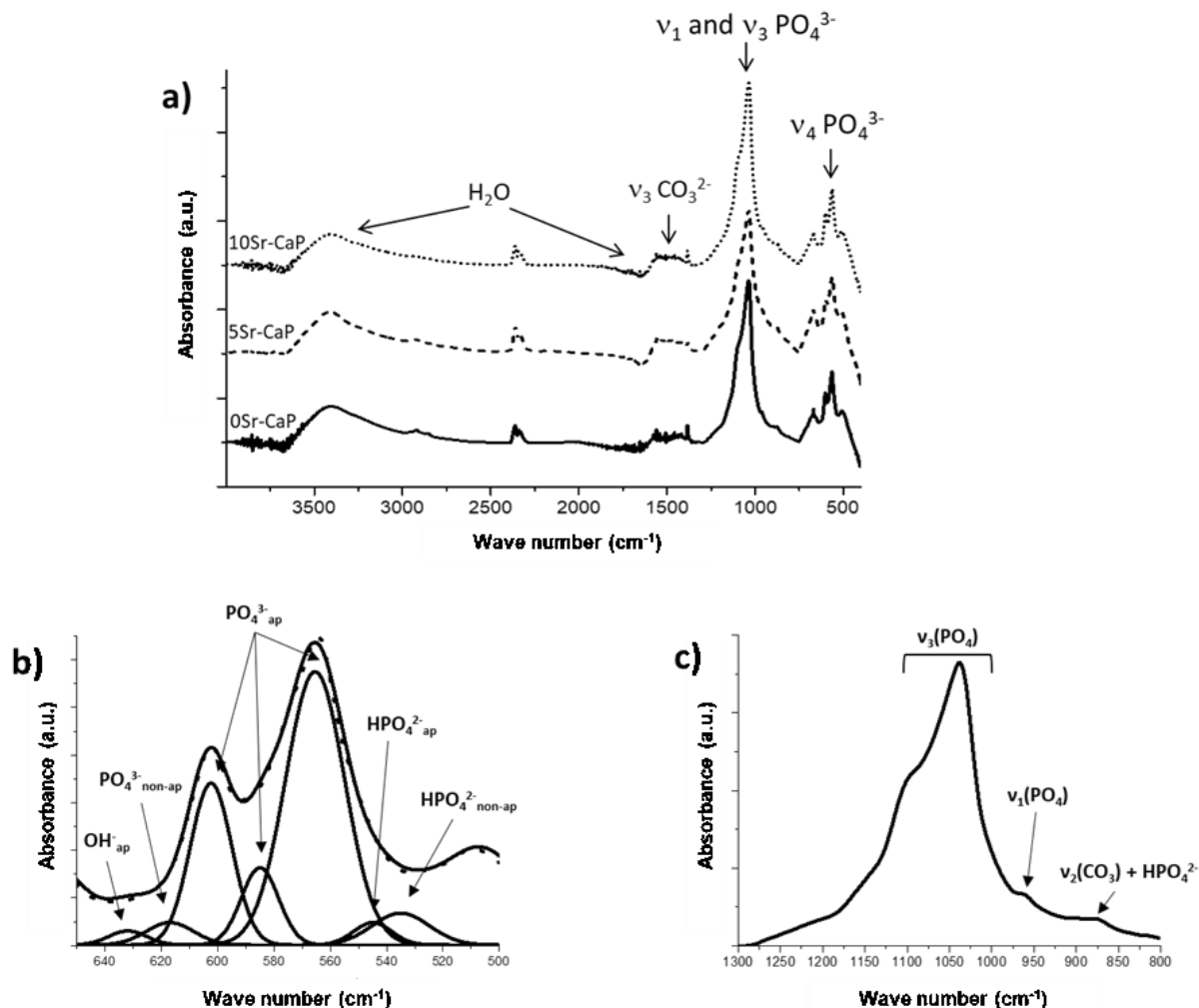


**Fig. 3.** (a) FTIR spectra of the  $x\text{Sr-CaP}$  materials (bottom-up: FM50K+0Sr-CaP; FM50K+5Sr-CaP; FM50K+10Sr-CaP, respectively); (b) detail of  $\nu_4$  mode of  $\text{PO}_4^{3-}$  domain with peak deconvolutions and (c) detail of  $\nu_1$  and  $\nu_3$  modes of the  $\text{PO}_4^{3-}$  domain. **(2-column fitting image)**

Characterization of the crystallographic structure of FM50K ACC without and with  $x\text{Sr-CaP}$  coatings was performed by X-ray diffraction and the corresponding diffractograms are given in Fig. 4. For the ACC material, the main diffraction peaks are located at  $2\theta \sim 23^\circ$ ,  $2\theta \sim 45^\circ$  and  $2\theta \sim 50^\circ$  (using  $\lambda K\alpha \text{ Cu} = 0.154056 \text{ nm}$ ), corresponding respectively to (002), (10) and (004) reflections of a carbon with a turbostratic structure [58]. The other peaks observed on this diffractogram are characteristic of the sizing and correspond to the zinc aluminate

(JCPDS n°: 39-473) present in the sizing composition. It is used as a surface treatment to enhance the fiber processability by preventing carbon fibers from breaking.

For the undoped CaP coating, the XRD diffractogram shows that the main diffraction peaks are located at  $2\theta = 26.08^\circ$ ,  $32.00^\circ$  and  $33.15^\circ$  corresponding respectively to (002), (211) and (300) reflections of the hexagonal hydroxyapatite (HA) structure (JCPDS no: 74-0566). Indexation of all diffraction peaks confirm the occurrence of only calcium-deficient hydroxyapatite (CDA) as unique crystalline phase. For the two strontium-doped coatings (5Sr-CaP and 10Sr-CaP), the XRD diffractograms are similar to that of the 0Sr-CaP coating, excepted that a shift of the main reflections towards lower  $2\theta^\circ$  values is observed when increasing the amount of strontium incorporated in the coating (Table 4). The lattice parameters ( $a$  and  $c$ ) of the undoped and Sr-doped CDA deposited phases were determined using the Debye refinement of the XRD diffractograms (after removing the ACC substrate contribution). The observed increase of these parameters,  $a$  from  $9.366 \text{ \AA}$  to  $9.379 \text{ \AA}$  and  $c$  from  $6.820 \text{ \AA}$  to  $6.834 \text{ \AA}$ , is consistent with a calcium/strontium substitution in the apatite structure (the ionic radii of Ca and Sr being  $1.00$  and  $1.18 \text{ \AA}$ , respectively). It could be noted that the relative increase of these parameters is slightly smaller than that reported for stoichiometric HA with the same Sr-doping obtained by precipitation [8] or high-temperature solid-state synthesis [59]. This may suggest that the amount of Sr incorporated in the coherent domains of the HA nanocrystals is weaker than that expected from chemical analyses.

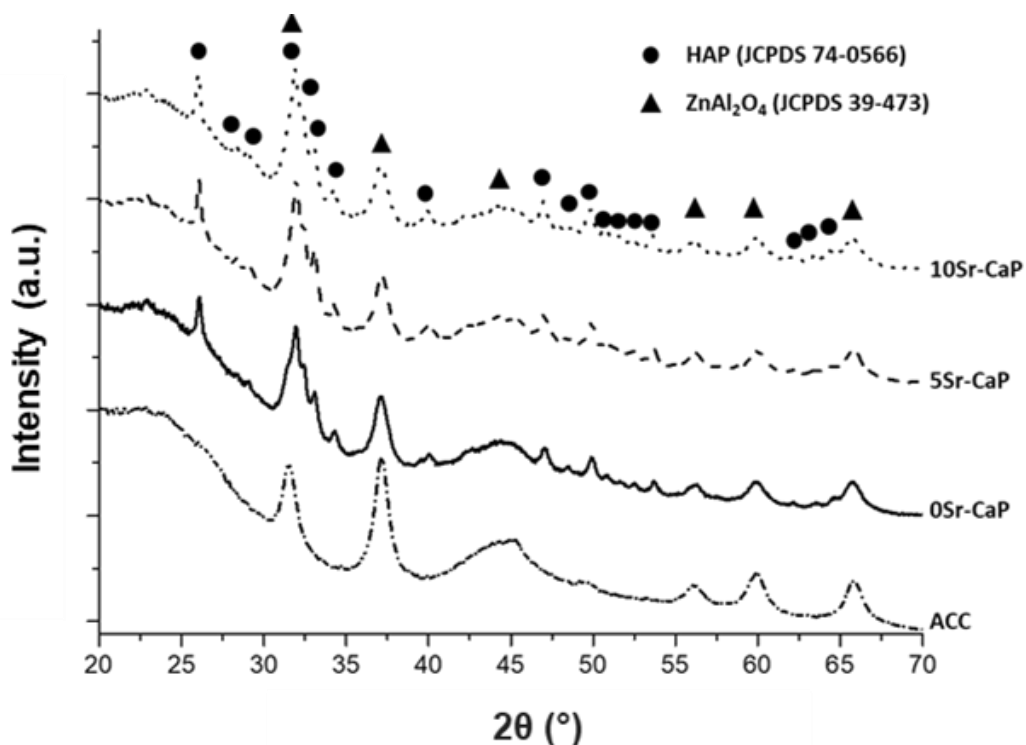


**Fig. 4.** XRD diffractograms of the pristine ACC and the ACC/xSr-CaP materials (bottom-up: FM50K; FM50K+0sr-CaP; FM50K+5sr-CaP; FM50K+10sr-CaP, respectively). **(2-column fitting image)**

**Table 4.** The XRD data:  $2\theta$  position of (002), (211) and (310) reflections for xSr-CaP coatings along with lattice parameters ( $\lambda K\alpha$  Cu = 0.154056nm).

Sample	(002)	(211)	(310)	Lattice parameters	
	Position, ( $2\theta^\circ$ )	Position, ( $2\theta^\circ$ )	Position, ( $2\theta^\circ$ )	a, ( $\text{\AA}$ )	c, ( $\text{\AA}$ )
0Sr-CaP	26.08	32.00	40.06	9.366	6.820
5Sr-CaP	26.05	31.97	40.03	-	-
10Sr-CaP	26.02	31.92	39.94	9.379	6.834

Further structural investigation of the xSr-CaP coatings was performed using solid-state  $^{31}\text{P}$  magic angle spinning (MAS) NMR spectroscopy. As shown in Fig. 5, the quantitative  $^{31}\text{P}$  MAS spectra of the three samples display an intense resonance located at 2.7-2.9 ppm typical of a carbonated nanocrystalline CDA [60–63] in agreement with FTIR and XRD results.  $^{31}\text{P}$ - $^1\text{H}$  cross-polarization (CP) MAS experiments performed at different contact times reveal that the observed lineshape contains two overlapping peaks, a main one (at 2.8 ppm for 0Sr-CaP coating) and a broader one of weaker intensity (at about 2.0 ppm for the 0Sr-CaP sample), as previously observed for nanocrystalline CDA and HA [62–64]. The  $^{31}\text{P}$

isotropic chemical shifts and linewidths of the two peaks, assigned to the ordered core of the nanoparticle and to a disordered non-apatitic surface layer respectively [63–66], were determined from simultaneous fits of CP-MAS spectra at different contact times and the obtained parameters were used to reconstruct the quantitative MAS spectra (see Fig. 5 (a), (b) and (c) where the thin green line is associated to apatitic  $\text{PO}_4^{3-}$  groups of the particle core, while the broad purple line corresponds to  $\text{PO}_4^{3-}$  and  $\text{HPO}_4^{2-}$  surface groups). When increasing the Sr-content, slight shifts of the narrow (from 2.8 to 2.9 ppm) and of the broad (from 2.0 to 2.2 ppm) peaks are observed, in agreement with previous studies [51]. A significant increase of the relative intensity of the broad peak is also observed for the Sr-doped coatings. This could suggest a preferential incorporation of Sr atoms in the disordered surface layer of the CDA nanoparticles and explain the moderate increase of cell parameters observed upon Sr-doping.

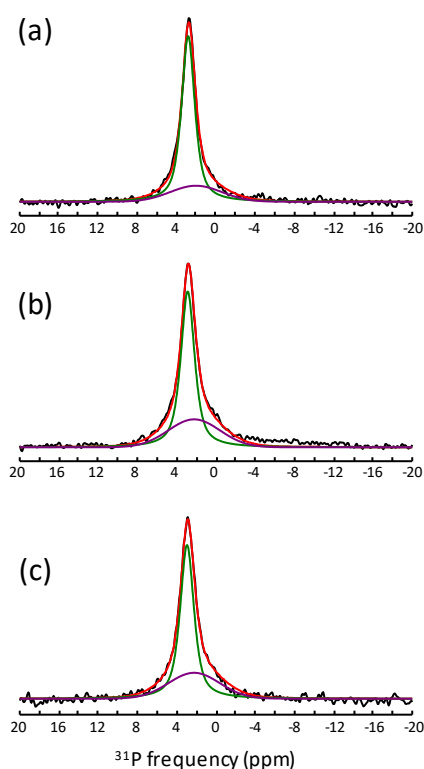


**Fig. 5.**  $^{31}\text{P}$  quantitative MAS NMR spectra of the ACC/xSr-CaP materials: a) 0Sr-CaP; b) 5Sr-CaP and c) 10Sr-CaP. Fits of experimental spectra are shown in red, the narrow peak assigned to the ordered core contribution and the broad one corresponding to the disordered surface layer are shown in green and purple. **(1-column fitting image + color)**

This assignment is supported by 2D  $^{31}\text{P}$ - $^1\text{H}$  heteronuclear correlation (HetCor) MAS NMR spectra, which allow deciphering the short-range proximities between P and H atoms. As shown in Fig. 6, the  $^{31}\text{P}$ - $^1\text{H}$  2D HetCor MAS spectra of the three coatings (cross-polarization contact time of 1 ms) exhibit an intense correlation peak between the main  $^{31}\text{P}$  resonance at 2.8-2.9 ppm and a narrow  $^1\text{H}$  resonance at 0 ppm characteristic of the  $\text{OH}^-$  hydroxyl ions of the apatitic structure. In addition, they show a broader correlation peak between the wider  $^{31}\text{P}$  contribution at a slightly smaller chemical shift (2.0-2.2 ppm) and broad  $^1\text{H}$  signals between 5 and 15 ppm corresponding to water molecules and  $\text{HPO}_4$  hydrogenophosphate ions. These features undoubtedly reveal that the undoped and Sr-doped CDA nanoparticles exhibit an ordered apatitic core and a disordered surface layer involving water molecules and non-apatitic  $\text{PO}_4^{3-}$  and  $\text{HPO}_4^{2-}$  groups [63–66], thereby showing similarities with bone mineral nanoparticles [65,66].

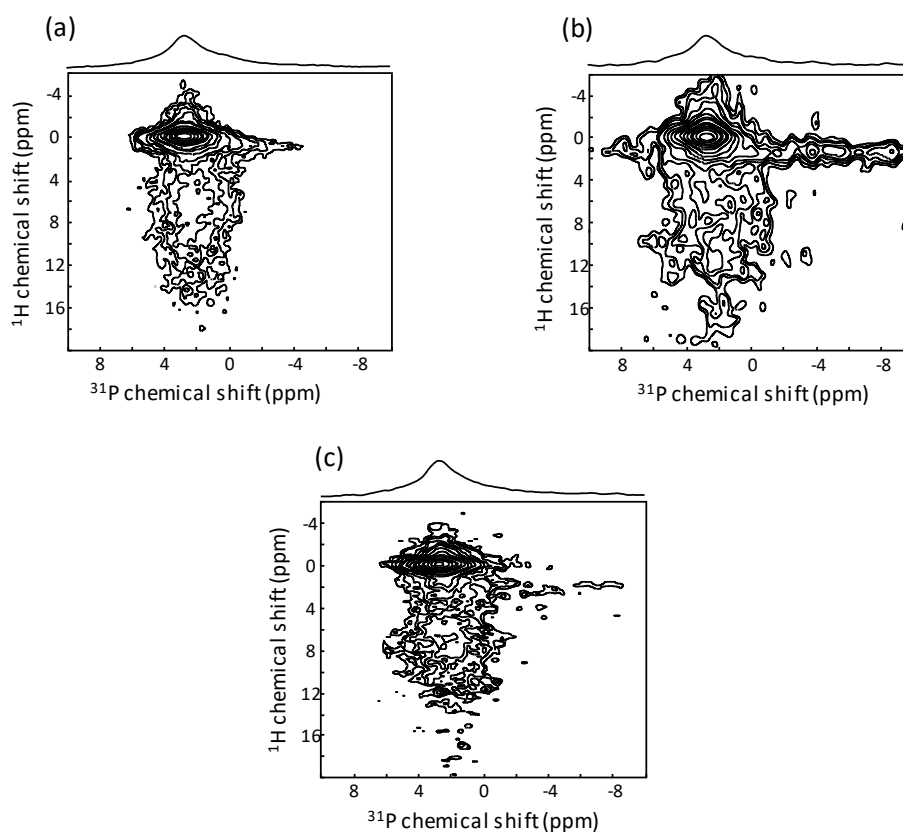


**Fig. 6.** Two-dimensional  $\{^1\text{H}\}^{31}\text{P}$  HetCor MAS NMR spectra of the sono-electrodeposition coatings: a) 0Sr-CaP; b) 5Sr-CaP and c) 10Sr-CaP. **(2-column fitting image)**

### 3.3. Biological characterization

Fluorescence analysis showed that human primary osteoblasts exhibited a fusiform shape along the ACC fibers (Fig. 7 (a) to (d)). After 2 and 4 days of culture of living cells (green fluorescence), very few dead cells (red fluorescence) were observed at the surface of the four materials. Cell enumeration (Fig. 7e) revealed that the cell density after 2 days was similar and statistically higher on FM50K ( $46 \pm 10$  cell/mm<sup>2</sup>), FM 50K+5Sr-CaP ( $35 \pm 10$  cell/mm<sup>2</sup>) and FM 50K+10Sr-CaP ( $35 \pm 10$  cell/mm<sup>2</sup>) compared to FM 50K+0Sr-CaP ( $19 \pm 3$  cell/mm<sup>2</sup>).

After 4 days, cell proliferation was observed on all materials, except on FM50K (from  $46 \pm 10$  to  $32 \pm 11$  cell/mm<sup>2</sup>, i.e. a decrease of 30%) and was the highest on strontium-doped materials, especially FM50K+10Sr-CaP.

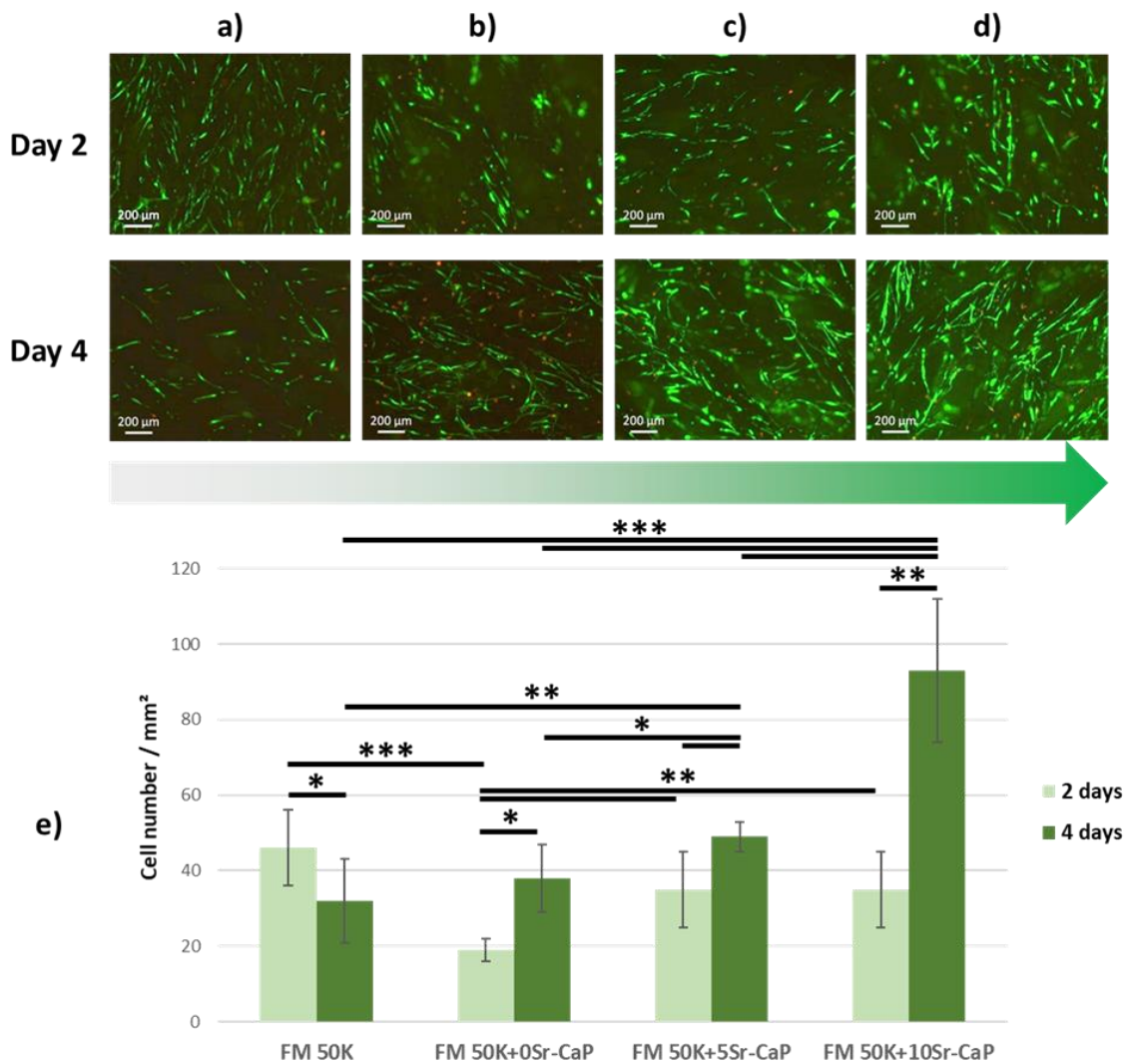


**Fig. 7. (a)-(d)** Typical fluorescence micrographs obtained after 2 and 4 days of culture of human primary osteoblasts on the four materials, namely FM 50K (a); FM 50K+0Sr-CaP (b); FM 50K+5Sr-CaP (c) and FM 50K+10Sr-CaP (d). Cell staining: live=green and dead=red. Mean  $\pm$  standard deviation, \*p < 0.05, \*\*p < 0.01 and \*\*\*p < 0.001. **e)** Quantification of cell number by mm<sup>2</sup> on the four materials after 2 and 4 days of culture using the ImageJ software. **(2-column fitting image + color)**

#### 4. Discussion

In the present study, FM50K activated carbon fiber cloth was chosen as a working electrode for its specific characteristics and properties, such as conductivity, hydrophilicity due to the presence of acidic groups on the ACC surface, and multi-scale porosity. We hypothesized that microporosity and hydrophilic properties would allow high ACC impregnation in aqueous electrolyte and that electrical conductivity would be optimal for CaP coating by sono-

electrodeposition. Our results established that FM50K-ACC was an appropriate substrate to obtain a uniform CaP coating with possible strontium substitution. The synthesis of strontium-substituted CaP coatings led to the expected final strontium range, i.e. between 3 and 7 at. % as based on previous studies. Interestingly, it was observed that the materials (xSr-CaP coated ACC substrate) were easy to handle allowing to perform all characterizations without damaging them. This also means that chemical bonds between xSr-CaP coatings and ACC fibers are tough enough.

It was relevant to analyze and then to compare the morphological, chemical and structural characteristics of the coatings, with and without strontium. Firstly, it is shown that strontium incorporation (< 10 at. %) does not modify the morphology and microtexture of xSr-CaP coatings. This leads to a uniform thickness (estimated around 1.5  $\mu\text{m}$ ) and a plate-like morphology. In TEM, whatever the materials, the coatings consist in lamellar nanocrystals which size is ranging from a few tens to a few hundreds of nanometers. Secondly, FTIR, XRD and solid-state NMR analyses reveal that the xSr-CaP coatings consist of carbonated CDA nanoparticles with an ordered apatitic core and a disordered hydrated surface layer. XRD data highlighted variations of cell parameters of the hexagonal crystallographic structure: *a* parameter increases from 9.366 Å to 9.379 Å and *c* parameter increases from 6.820 Å to 6.834 Å. This is an evidence of a calcium/strontium substitution in the coherent domains of the HA nanocrystals. It is confirmed by the  $^{31}\text{P}$  MAS spectra of the xSr-CaP coatings which suggest that the Sr atoms are incorporated into both the core and the disordered surface layer of the CDA nanoparticles.

This incorporation mechanism is expected to lead to different Sr release rates in solution or *in vivo* since the Sr cations located in the hydrated disordered layer are loosely bound and can be more easily exchanged in solution than those incorporated into the more ordered core of the nanoparticles [67]. Biological experiments revealed that ACC and CaP coated ACC are biocompatible. However, ACC substrate without any coating does not favor osteoblast proliferation, hence the interest of CaP coating. It is worth noting that the best proliferation

rate is obtained with the highest Sr-substituted CaP coating. This result is consistent with previous studies showing the benefit of using Sr to increase bone regeneration [16].

## **5. Conclusion**

The originality of the present study concerns the incorporation of a strontium cation into a biomimetic apatite coating deposited on conductive ACC material by sono-electrodeposition. This process is an interesting and efficient technique to deposit a strontium-substituted carbonated CDA coating on a carbon fiber cloth. A single crystalline Sr-CaP phase is obtained, in which calcium and strontium cations occupy similar positions in the apatitic lattice. The substitution of calcium by strontium ions, having a different ionic radius and electronegativity, leads to slight structural modifications of the CDA phase but does not modify the nanocrystal organization or the microtexture of the CDA coatings. The coatings display a plate-like morphology consisting of lamellar nanocrystals of carbonated CDA. The structure of the nanocrystals comprises an apatitic ordered core and a non-apatitic disordered and hydrated surface layer, typical of a biomimetic apatite. After hybrid material synthesis and characterization, cell viability assays were performed on human primary osteoblast cells, cultured on the carbon fiber cloth substrate without and with xSr-CaP coatings. As these materials show a strong affinity with human primary osteoblasts, the incorporation of strontium in the CDA phase structure has a beneficial role on cell proliferation.

## **Acknowledgements**

This work was financially supported by the FP7-IRSES European program “ABREM” 2012–2015, the Region Centre-Val de Loire projects “MatBioReOs” 2014–2017 and “MatCCaPBio” 2018-20210.

The authors are grateful to K. Beck for mercury porosity, R. Nehmé for assistance in MP-AES experiments, A. Richard for the SEM images, F. Warmont for the TEM images and E. Verron for calculating the hydroxyapatite lattice parameters.

## References

- [1] J. Gómez-Morales, M. Lafisco, J.M. Delgado-López, S. Sarda, C. Drouet, Progress on the preparation of nanocrystalline apatites and surface characterization: Overview of fundamental and applied aspects, *Prog. Cryst. Growth Charact. Mater.* 59 (2013) 1–46. <https://doi.org/10.1016/j.pcrysgrow.2012.11.001>.
- [2] L.D. Quarles, Cation Sensing Receptors in Bone: A Novel Paradigm for Regulating Bone Remodeling?, *J. Bone Miner. Res.* 12 (1997) 1971–1974. <https://doi.org/10.1359/jbmr.1997.12.12.1971>.
- [3] D. Laurencin, N. Almora-Barrios, N.H. de Leeuw, C. Gervais, C. Bonhomme, F. Mauri, W. Chrzanowski, J.C. Knowles, R.J. Newport, A. Wong, Z. Gan, M.E. Smith, Magnesium incorporation into hydroxyapatite, *Biomaterials.* 32 (2011) 1826–1837. <https://doi.org/10.1016/j.biomaterials.2010.11.017>.
- [4] X. Lijuan, J. Liuyun, X. Chengdong, J. Lixin, Effect of different synthesis conditions on the microstructure, crystallinity and solubility of Mg-substituted hydroxyapatite nanopowder, *Adv. Powder Technol.* 25 (2014) 1142–1146. <https://doi.org/10.1016/j.apt.2014.02.019>.
- [5] S.C. Cox, P. Jamshidi, L.M. Grover, K.K. Mallick, Preparation and characterisation of nanophase Sr, Mg, and Zn substituted hydroxyapatite by aqueous precipitation, *Mater. Sci. Eng. C.* 35 (2014) 106–114. <https://doi.org/10.1016/j.msec.2013.10.015>.
- [6] J. Abert, C. Bergmann, H. Fischer, Wet chemical synthesis of strontium-substituted hydroxyapatite and its influence on the mechanical and biological properties, *Ceram. Int.* 40 (2014) 9195–9203. <https://doi.org/10.1016/j.ceramint.2014.01.138>.
- [7] M. Šupová, Substituted hydroxyapatites for biomedical applications: A review, *Ceram. Int.* 41 (2015) 9203–9231. <https://doi.org/10.1016/j.ceramint.2015.03.316>.
- [8] M. Frasnelli, F. Cristofaro, V.M. Sglavo, S. Dirè, E. Callone, R. Ceccato, G. Bruni, A.I. Cornaglia, L. Visai, Synthesis and characterization of strontium-substituted hydroxyapatite nanoparticles for bone regeneration, *Mater. Sci. Eng. C.* 71 (2017) 653–662. <https://doi.org/10.1016/j.msec.2016.10.047>.
- [9] R.D. Shannon, Revised Effective Ionic Radii and Systematic Studies of Interatomic Distances in Halides and Chalcogenides, *Acta Cryst. A* 32 (1976) 751–767.
- [10] Z.Y. Li, W.M. Lam, C. Yang, B. Xu, G.X. Ni, S.A. Abbah, K.M.C. Cheung, K.D.K. Luk, W.W. Lu, Chemical composition, crystal size and lattice structural changes after incorporation of strontium into biomimetic apatite, *Biomaterials.* 28 (2007) 1452–1460. <https://doi.org/10.1016/j.biomaterials.2006.11.001>.
- [11] C. Drouet, M.-T. Carayon, C. Combes, C. Rey, Surface enrichment of biomimetic apatites with biologically-active ions Mg<sup>2+</sup> and Sr<sup>2+</sup>: A preamble to the activation of bone repair materials, *Mater. Sci. Eng. C.* 28 (2008) 1544–1550. <https://doi.org/10.1016/j.msec.2008.04.011>.
- [12] E. Boanini, M. Gazzano, A. Bigi, Ionic substitutions in calcium phosphates synthesized at low temperature, *Acta Biomater.* 6 (2010) 1882–1894. <https://doi.org/10.1016/j.actbio.2009.12.041>.
- [13] Z. Leilei, L. Hejun, L. Kezhi, Z. Shouyang, F. Qiangang, Z. Yulei, L. Shoujie, Double-layer TC4/Sr substituted hydroxyapatite bioactive coating for carbon/carbon composites, *Ceram. Int.* 41 (2015) 427–435. <https://doi.org/10.1016/j.ceramint.2014.08.087>.
- [14] W. Querido, A.L. Rossi, M. Farina, The effects of strontium on bone mineral: A review on current knowledge and microanalytical approaches, *Micron.* 80 (2016) 122–134. <https://doi.org/10.1016/j.micron.2015.10.006>.
- [15] C. Capuccini, P. Torricelli, E. Boanini, M. Gazzano, R. Giardino, A. Bigi, Interaction of Sr-doped hydroxyapatite nanocrystals with osteoclast and osteoblast-like cells, *J. Biomed. Mater. Res. A.* 89A (2009) 594–600. <https://doi.org/10.1002/jbm.a.31975>.
- [16] C. Capuccini, P. Torricelli, F. Sima, E. Boanini, C. Ristoscu, B. Bracci, G. Socol, M. Fini, I.N. Mihailescu, A. Bigi, Strontium-substituted hydroxyapatite coatings synthesized by pulsed-laser deposition: In vitro osteoblast and osteoclast response, *Acta Biomater.* 4 (2008) 1885–1893. <https://doi.org/10.1016/j.actbio.2008.05.005>.

- [17] S. Panzavolta, P. Torricelli, S. Casolari, A. Parrilli, M. Fini, A. Bigi, Strontium-Substituted Hydroxyapatite-Gelatin Biomimetic Scaffolds Modulate Bone Cell Response, *Macromol. Biosci.* 18 (2018) 1800096. <https://doi.org/10.1002/mabi.201800096>.
- [18] G. Boivin, P. Deloffre, B. Perrat, G. Panczer, M. Boudeulle, Y. Mauras, P. Allain, Y. Tsouderos, P.J. Meunier, Strontium distribution and interactions with bone mineral in monkey iliac bone after strontium salt (S 12911) administration, *J. Bone Miner. Res.* 11 (1996) 1302–1311. <https://doi.org/10.1002/jbmr.5650110915>.
- [19] S.C. Verberckmoes, M.E. De Broe, P.C. D'Haese, Dose-dependent effects of strontium on osteoblast function and mineralization, *Kidney Int.* 64 (2003) 534–543. <https://doi.org/10.1046/j.1523-1755.2003.00123.x>.
- [20] C. Bussola Tovani, A. Gloter, T. Azaïs, M. Selmane, A.P. Ramos, N. Nassif, Formation of stable strontium-rich amorphous calcium phosphate: Possible effects on bone mineral, *Acta Biomater.* 92 (2019) 315–324. <https://doi.org/10.1016/j.actbio.2019.05.036>.
- [21] E. Landi, A. Tampieri, G. Celotti, S. Sprio, M. Sandri, G. Logroscino, Sr-substituted hydroxyapatites for osteoporotic bone replacement, *Acta Biomater.* 3 (2007) 961–969. <https://doi.org/10.1016/j.actbio.2007.05.006>.
- [22] Y. Shen, J. Liu, K. Lin, W. Zhang, Synthesis of strontium substituted hydroxyapatite whiskers used as bioactive and mechanical reinforcement material, *Mater. Lett.* 70 (2012) 76–79. <https://doi.org/10.1016/j.matlet.2011.11.093>.
- [23] G. Renaudin, E. Jallot, J.M. Nedelec, Effect of strontium substitution on the composition and microstructure of sol–gel derived calcium phosphates, *J. Sol-Gel Sci. Technol.* 51 (2009) 287–294. <https://doi.org/10.1007/s10971-008-1854-5>.
- [24] S.A. Qaisar, M. Bilton, Wallace, R., Brydson, R., Brown, A. P., Ward, M., Milne, S. J., Sol-gel synthesis and TEM-EDX characterisation of hydroxyapatite nanoscale powders modified by Mg, Sr or Ti, *J. Phys. Conf. Ser.* 241 (2010) 012052. <https://doi.org/10.1088/1742-6596/241/1/012052>.
- [25] M.D. O'Donnell, Y. Fredholm, A. de Rouffignac, R.G. Hill, Structural analysis of a series of strontium-substituted apatites, *Acta Biomater.* 4 (2008) 1455–1464. <https://doi.org/10.1016/j.actbio.2008.04.018>.
- [26] K. Lin, P. Liu, L. Wei, Z. Zou, W. Zhang, Y. Qian, Y. Shen, J. Chang, Strontium substituted hydroxyapatite porous microspheres: Surfactant-free hydrothermal synthesis, enhanced biological response and sustained drug release, *Chem. Eng. J.* 222 (2013) 49–59. <https://doi.org/10.1016/j.cej.2013.02.037>.
- [27] C.-J. Chung, H.-Y. Long, Systematic strontium substitution in hydroxyapatite coatings on titanium via micro-arc treatment and their osteoblast/osteoclast responses, *Acta Biomater.* 7 (2011) 4081–4087. <https://doi.org/10.1016/j.actbio.2011.07.004>.
- [28] I. Pereiro, C. Rodríguez-Valencia, C. Serra, E.L. Solla, J. Serra, P. González, Pulsed laser deposition of strontium-substituted hydroxyapatite coatings, *Appl. Surf. Sci.* 258 (2012) 9192–9197. <https://doi.org/10.1016/j.apsusc.2012.04.063>.
- [29] Y. Huang, Q. Ding, X. Pang, S. Han, Y. Yan, Corrosion behavior and biocompatibility of strontium and fluorine co-doped electrodeposited hydroxyapatite coatings, *Appl. Surf. Sci.* 282 (2013) 456–462. <https://doi.org/10.1016/j.apsusc.2013.05.152>.
- [30] R. Drevet, H. Benhayoune, Pulsed electrodeposition for the synthesis of strontium-substituted calcium phosphate coatings with improved dissolution properties, *Mater. Sci. Eng. C.* 33 (2013) 4260–4265. <https://doi.org/10.1016/j.msec.2013.06.019>.
- [31] M. Røkkum, A. Reigstad, Total hip replacement with an entirely hydroxyapatite-coated prosthesis: 5 years' follow-up of 94 consecutive hips, *J. Arthroplasty.* 14 (1999) 689–700. [https://doi.org/10.1016/S0883-5403\(99\)90224-3](https://doi.org/10.1016/S0883-5403(99)90224-3).
- [32] A. Rogers, R. Kulkarni, E.M. Downes, The ABG hydroxyapatite-coated hip prosthesis: One hundred consecutive operations with average 6-year follow-up, *J. Arthroplasty.* 18 (2003) 619–625. [https://doi.org/10.1016/S0883-5403\(03\)00208-0](https://doi.org/10.1016/S0883-5403(03)00208-0).
- [33] D. Gopi, J. Indira, L. Kavitha, A comparative study on the direct and pulsed current electrodeposition of hydroxyapatite coatings on surgical grade stainless steel, *Surf. Coat. Technol.* 206 (2012) 2859–2869. <https://doi.org/10.1016/j.surfcoat.2011.12.011>.

- [34]N. Dumelie, H. Benhayoune, D. Richard, D. Laurent-Maquin, G. Balossier, In vitro precipitation of electrodeposited calcium-deficient hydroxyapatite coatings on Ti6Al4V substrate, *Mater. Charact.* 59 (2008) 129–133. <https://doi.org/10.1016/j.matchar.2006.11.030>.
- [35]N. Eliaz, M. Eliyahu, Electrochemical processes of nucleation and growth of hydroxyapatite on titanium supported by real-time electrochemical atomic force microscopy, *J. Biomed. Mater. Res. A.* 80A (2007) 621–634. <https://doi.org/10.1002/jbm.a.30944>.
- [36]R. Walter, M. Bobby Kannan, Y. He, A. Sandham, Influence of the cathodic activity of magnesium alloys on the electrochemical deposition of calcium phosphate, *Mater. Lett.* 130 (2014) 184–187. <https://doi.org/10.1016/j.matlet.2014.05.125>.
- [37]Y. Yan, A. Neville, D. Dowson, S. Williams, J. Fisher, Effect of metallic nanoparticles on the biotribocorrosion behaviour of Metal-on-Metal hip prostheses, 17th Int. Conf. Wear *Mater.* 267 (2009) 683–688. <https://doi.org/10.1016/j.wear.2008.12.110>.
- [38]S.R. Sandeman, H. Jeffery, C.A. Howell, M. Smith, S.V. Mikhalovsky, A.W. Lloyd, The in vitro corneal biocompatibility of hydroxyapatite coated carbon mesh, *Biomaterials.* 30 (2009) 3143–3149. <https://doi.org/10.1016/j.biomaterials.2009.02.042>.
- [39]D. Adams, D.F. Williams, J. Hill, Carbon fiber-reinforced carbon as a potential implant material, *J. Biomed. Mater. Res.* 12 (1978) 35–42. <https://doi.org/10.1002/jbm.820120104>.
- [40]R.J. Minns, D.S. Muckle, J.E. Donkin, The repair of osteochondral defects in osteoarthritic rabbit knees by the use of carbon fibre, *Biomaterials.* 3 (1982) 81–86. [https://doi.org/10.1016/0142-9612\(82\)90038-2](https://doi.org/10.1016/0142-9612(82)90038-2).
- [41]R.J. Minns, D.S. Muckle, Mechanical and histological response of carbon fibre pads implanted in the rabbit patella, *Biomaterials.* 10 (1989) 273–276. [https://doi.org/10.1016/0142-9612\(89\)90105-1](https://doi.org/10.1016/0142-9612(89)90105-1).
- [42]S.E. Mäkisalo, P. Paavolainen, M. Grönblad, T. Holmström, Tissue reactions around two alloplastic ligament substitute materials: experimental study on rats with carbon fibres and polypropylene, *Biomaterials.* 10 (1989) 105–108. [https://doi.org/10.1016/0142-9612\(89\)90041-0](https://doi.org/10.1016/0142-9612(89)90041-0).
- [43]A. Carranza-Bencano, J.R. Armas-Padro, Carbon fiber implants in osteochondral defects of the rabbit patella, (2000) 6.
- [44]A. Slosarczyk, M. Klisch, M. Blazewicz, J. Piekarczyk, L. Stobierski, A. Rapacz-Kmita, Hot pressed hydroxyapatite-carbon fibre composites, *J. Eur. Ceram. Soc.* (2000) 1397–1402.
- [45]M. Wu, Q. Wang, X. Liu, H. Liu, Biomimetic synthesis and characterization of carbon nanofiber/hydroxyapatite composite scaffolds, *Carbon.* 51 (2013) 335–345. <https://doi.org/10.1016/j.carbon.2012.08.061>.
- [46]X. Wang, X. Zhao, L. Zhang, W. Wang, J. Zhang, F. He, J. Yang, Design and fabrication of carbon fibers with needle-like nano-HA coating to reinforce granular nano-HA composites, *Mater. Sci. Eng. C.* 77 (2017) 765–771. <https://doi.org/10.1016/j.msec.2017.03.307>.
- [47]X. Zhao, X. Wang, H. Xin, L. Zhang, J. Yang, G. Jiang, Controllable preparation of SiC coating protecting carbon fiber from oxidation damage during sintering process and SiC coated carbon fiber reinforced hydroxyapatite composites, *Appl. Surf. Sci.* 450 (2018) 265–273. <https://doi.org/10.1016/j.apsusc.2018.04.164>.
- [48]X. Wang, X. Zhao, W. Wang, J. Zhang, L. Zhang, F. He, J. Yang, Controllable preparation of a nano-hydroxyapatite coating on carbon fibers by electrochemical deposition and chemical treatment, *Mater. Sci. Eng. C.* 63 (2016) 96–105. <https://doi.org/10.1016/j.msec.2016.02.058>.
- [49]H. Hong-mei, S.V. Mikhalovsky, G.J. Phillips, A.W. Lloyd, Calcium phosphate sono-electrodeposition on carbon fabrics and its effect on osteoblast cell viability in vitro, *New Carbon Mater.* (2007) 5.
- [50]F. Olivier, Q. Picard, S. Delpoux-Ouldriane, J. Chancolon, F. Warmont, V. Sarou-Kanian, F. Fayon, S. Bonnamy, Influence of electrochemical parameters on the characteristics of

- sono-electrodeposited calcium phosphate-coated carbon fiber cloth, *Surf. Coat. Technol.* 389 (2020) 125507. <https://doi.org/10.1016/j.surfcoat.2020.125507>.
- [51] A. Bigi, E. Boanini, C. Capuccini, M. Gazzano, Strontium-substituted hydroxyapatite nanocrystals, *Inorganica Chim. Acta.* 360 (2007) 1009–1016. <https://doi.org/10.1016/j.ica.2006.07.074>.
- [52] C. Rey, C. Combes, C. Drouet, H. Sfihi, A. Barroug, Physico-chemical properties of nanocrystalline apatites: Implications for biominerals and biomaterials, *Mater. Sci. Eng. C.* 27 (2007) 198–205. <https://doi.org/10.1016/j.msec.2006.05.015>.
- [53] N. Vandecandelaere, C. Rey, C. Drouet, Biomimetic apatite-based biomaterials: on the critical impact of synthesis and post-synthesis parameters, *J. Mater. Sci. Mater. Med.* 23 (2012) 2593–2606. <https://doi.org/10.1007/s10856-012-4719-y>.
- [54] C. Rey, M. Shimizu, B. Collins, M.J. Glimcher, Resolution-enhanced fourier transform infrared spectroscopy study of the environment of phosphate ion in the early deposits of a solid phase of calcium phosphate in bone and enamel and their evolution with age: 2. Investigations in the  $\nu_3$  PO<sub>4</sub> domain, *Calcif. Tissue Int.* 49 (1991) 383–388. <https://doi.org/10.1007/BF02555847>.
- [55] C. Rey, C. Combes, C. Drouet, D. Grossin, *Bioactive Ceramics: Physical Chemistry*, in: *Compr. Biomater.*, Elsevier, 2011: pp. 187–221. <https://doi.org/10.1016/B978-0-08-055294-1.00178-1>.
- [56] C. Rey, B. Collins, T. Goehl, I.R. Dickson, M.J. Glimcher, The carbonate environment in bone mineral: A resolution-enhanced fourier transform infrared spectroscopy study, *Calcif. Tissue Int.* 45 (1989) 157–164. <https://doi.org/10.1007/BF02556059>.
- [57] C.G. Weber, M. Mueller, N. Vandecandelaere, I. Trick, A. Burger-Kentischer, T. Maucher, C. Drouet, Enzyme-functionalized biomimetic apatites: concept and perspectives in view of innovative medical approaches, *J. Mater. Sci. Mater. Med.* 25 (2014) 595–606. <https://doi.org/10.1007/s10856-013-5097-9>.
- [58] A. Oberlin, S. Bonnamy, K. Oshida, Landmarks for graphitization, *TANSO.* 2006 (2006) 281–298. <https://doi.org/10.7209/tanso.2006.281>.
- [59] A. Bigi, G. Falini, M. Gazzano, N. Roveri, E. Tedesco, Structural Refinements of Strontium Substituted Hydroxylapatites, *Mater. Sci. Forum.* 278–281 (1998) 814–819. <https://doi.org/10.4028/www.scientific.net/MSF.278-281.814>.
- [60] R.N. Panda, M.F. Hsieh, R.J. Chung, T.S. Chin, FTIR, XRD, SEM and solid state NMR investigations of carbonate-containing hydroxyapatite nano-particles synthesized by hydroxide-gel technique, *J. Phys. Chem. Solids.* 64 (2003) 193–199. [https://doi.org/10.1016/S0022-3697\(02\)00257-3](https://doi.org/10.1016/S0022-3697(02)00257-3).
- [61] W.P. Aue, A.H. Roufosse, M.J. Glimcher, R.G. Griffin, Solid-state phosphorus-31 nuclear magnetic resonance studies of synthetic solid phases of calcium phosphate: potential models of bone mineral, *Biochemistry.* 23 (1984) 6110–6114. <https://doi.org/10.1021/bi00320a032>.
- [62] H. Roussière, G. Montavon, S. Laïb, P. Janvier, B. Alonso, F. Fayon, M. Petit, D. Massiot, J.-M. Bouler, B. Bujoli, Hybrid materials applied to biotechnologies: coating of calcium phosphates for the design of implants active against bone resorption disorders, *J. Mater. Chem.* 15 (2005) 3869. <https://doi.org/10.1039/b503680a>.
- [63] C. Mellier, F. Fayon, F. Boukhechba, E. Verron, M. LeFerrec, G. Montavon, J. Lesoeur, V. Schnitzler, D. Massiot, P. Janvier, O. Gauthier, J.-M. Bouler, B. Bujoli, Design and properties of novel gallium-doped injectable apatitic cements, *Acta Biomater.* 24 (2015) 322–332. <https://doi.org/10.1016/j.actbio.2015.05.027>.
- [64] C. Jäger, T. Welzel, W. Meyer-Zaika, M. Epple, A solid-state NMR investigation of the structure of nanocrystalline hydroxyapatite, *Magn. Reson. Chem.* 44 (2006) 573–580. <https://doi.org/10.1002/mrc.1774>.
- [65] Y. Wang, S. Von Euw, F.M. Fernandes, S. Cassaignon, M. Selmane, G. Laurent, G. Pehau-Arnaudet, C. Coelho, L. Bonhomme-Coury, M.-M. Giraud-Guille, F. Babonneau, T. Azaïs, N. Nassif, Water-mediated structuring of bone apatite, *Nat. Mater.* 12 (2013) 1144–1153. <https://doi.org/10.1038/nmat3787>.

- [66] S. Von Euw, W. Ajili, T.-H.-C. Chan-Chang, A. Delices, G. Laurent, F. Babonneau, N. Nassif, T. Azaïs, Amorphous surface layer versus transient amorphous precursor phase in bone – A case study investigated by solid-state NMR spectroscopy, *Acta Biomater.* 59 (2017) 351–360. <https://doi.org/10.1016/j.actbio.2017.06.040>.
- [67] S. Cazalbou, D. Eichert, X. Ranz, C. Drouet, C. Combes, M.F. Harmand, C. Rey, Ion exchanges in apatites for biomedical applications, 16 (2005) 405–409.